Supplement of Weather Clim. Dynam., 5, 537–557, 2024
https://doi.org/10.5194/wcd-5-537-2024-supplement
© Author(s) 2024. CC BY 4.0 License.

Supplement of

Warm conveyor belt characteristics and impacts along the life cycle of extratropical cyclones: case studies and climatological analysis based on ERA5

Katharina Heitmann et al.

Correspondence to: Katharina Heitmann (katharina.heitmann@env.ethz.ch)

The copyright of individual parts of the supplement might differ from the article licence.

S1 Case 2: January 1989, ERICA IOP4, North Atlantic

The Experiment on Rapidly Intensifying Cyclones over the Atlantic (ERICA) took place at the beginning of 1989. During the fourth period of intense observations (IOP4), a cyclone formed off the US east coast and later developed into the most extreme cyclone in this region until then, with a minimum SLP of 936 hPa, and a deepening rate of 3.4 Bergeron, as described by Neiman and Shapiro (1993). The latter study, along with Neiman et al. (1993), provides a detailed description and analysis of the development of the frontal structures of this cyclone. The latter study described the associated WCB as a southerly airstream that ascended over the warm front during the early phase of cyclogenesis. Doppler-radar cross sections of the vertical velocity and reflectivity at the warm front at 06 UTC on 4 January 1989 showed that the WCB consisted of a combination of rapidly and slowly ascending sub-airstreams, which Neiman et al. (1993) referred to as "elevator vs. escalator" ascent. While the life cycle of the ERICA IOP4 cyclone is well documented, the temporal evolution of the associated WCB has not been investigated. In the following, we describe the characteristics and impacts of this WCB at individual time steps and investigate their evolution along the cyclone life cycle.

S1.1 WCB characteristics

Figure S1 shows all WCB trajectories associated with the ERICA IOP4 cyclone that contributed to the WCB ascent mask at two specific time steps. At 00 UTC on 4 January 1989 (Fig. S1a), the weak cyclone is located off the US east coast and ahead of a relatively broad upper-level trough (indicated by the 2-pvu contour on 320 K). The 209 trajectories that define the associated WCB ascent mask originate over the southeastern US and ascend gradually from west to east (Fig. S1a). During their main ascent phase, the WCB turns northeastward and mainly remains a coherent bundle of trajectories. The position of the trajectories at this moment in time (indicated by black dots in Fig. S1a) coincides with the location of the developing cyclone. Later, in the WCB outflow, the trajectories turn eastward along the upper-level flow.

During the next 18 h, the cyclone intensifies strongly while moving eastward, and the upper-level trough wraps up cyclonically (cyclonic wave breaking, Thorncroft et al., 1993). At 18 UTC on 4 January (Fig. S1b), 579 trajectories contribute to the WCB ascent mask, i.e., the WCB more than doubled its intensity. Some of these trajectories still originate from the southeastern US, but most have their starting positions in the western North Atlantic. In contrast to the situation 18 h before, the WCB trajectories turn poleward during their ascent and strongly diverge at upper levels. Most WCB trajectories ascend rapidly near the cyclone center, while some trajectories ascend along the cold front. The WCB ascent mask (given by the envelope of the black dots in Fig. S1b) nicely agrees with the T-bone frontal structure described by Neiman et al. (1993), with a short warm, and prominent bent-back front. At this time, the WCB outflow reaches much more poleward than 18 h before, contributing to the formation of a prominent ridge downstream of the cyclone. Similar to the situation at 00 UTC on 4 January, the trajectories turn anticyclonically at upper levels, and some trajectories descend slightly towards Europe. Thus, by examining the WCB at two individual time steps 18 h apart, we can already observe a qualitative shift in the characteristics of the WCB.

S1.2 WCB impacts

We now investigate the precipitation rate and low-level PV in the region of the WCB ascent as well as the upper-level PV anomaly in the region of the WCB outflow at selected time steps along the cyclone life cycle. Early in the life cycle, at 00 UTC on 4 January (Fig. S2a), the cyclone is associated with weak precipitation mainly near the center and south of it in the warm sector. The precipitation signal aligns almost perfectly with the WCB ascent mask (red contour in Fig. S2a and black dots in Fig. S1a). During the following 18 h, when the cyclone and WCB both strongly intensify, precipitation also becomes considerably more intense. At 18 UTC on 4 January (Fig. S2b), the most intense precipitation occurs northeast of the cyclone center and along the cold front ($> 4\,\mathrm{mm\,h^{-1}}$). Again, the vast majority of precipitation occurs inside the WCB ascent mask. Weak precipitation rates behind the cold front are not associated with the WCB ascent (most likely shallow cumulus convection in the cold sector). A day later, at 18 UTC on 5 January (Fig. S2c), the cyclone center has moved poleward and has been overtaken by the upper-level trough, and the WCB ascends mainly along the elongated cold front. Precipitation is strongest along the cold front inside the WCB ascent mask, and precipitation near the cyclone center has strongly decreased.

At 00 UTC on 4 January (Fig. S2d), the region of the cyclone is characterized by low PV values at low levels (750–950 hPa), indicating weak diabatic PV production at this point. After the strong cyclone intensification in the following 18 h, a region

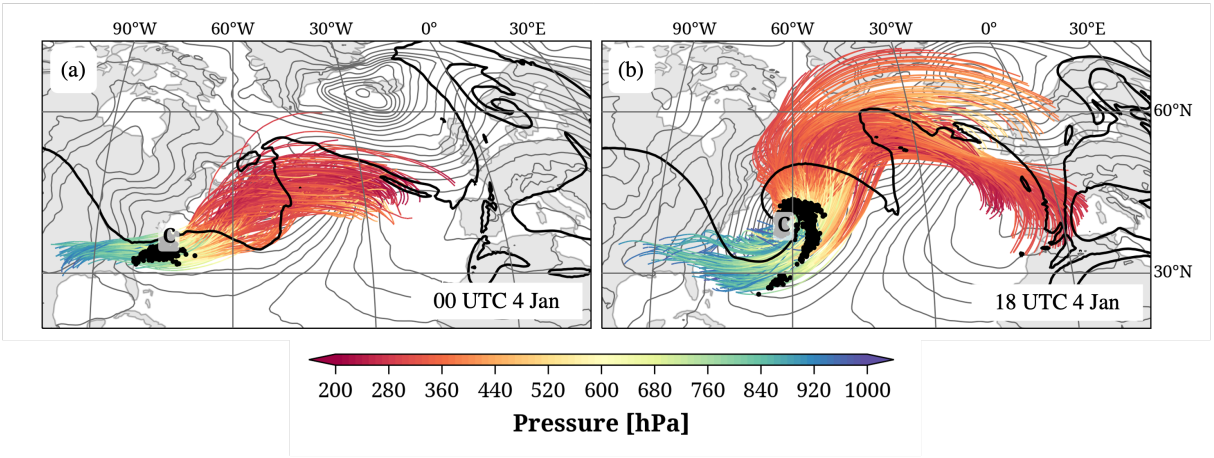

Figure S1. 48-hour WCB trajectories (colored by pressure; hPa) associated with Case 1 (ERICA IOP4 cyclone). Trajectories are shown that contribute to the WCB ascent mask (500–800 hPa) at (a) 00 UTC and (b) 18 UTC on 4 January 1989. The position of the WCB air parcels (black dots), SLP (every 4 hPa, grey contours), the 2-pvu contour at 320 K (black dashed line) and the position of the cyclone center (letter 'C') are shown at the respective time step.

of enhanced low-level PV (> 2.5 pvu) is located along the bent-back front, within the WCB ascent (Fig. S2e). We note that the intense signal of PV at low levels along the bent-back front (Fig. S2e) agrees well with the observation-based analyses in Neiman et al. (1993) who showed very intense low-level PV in this region associated with a westerly low-level jet exceeding $35\,\mathrm{m\,s^{-1}}$ (their Fig. 18). In contrast, the region of the WCB ascent along the cold front does not show enhanced low-level PV values. After the cyclone intensification, PV values remain high near the cyclone center, where a small fraction of the WCB ascends (Fig. S2f). In addition, the elongated region of the WCB ascent along the cold front is also associated with enhanced low-level PV values. At this moment, regions of enhanced precipitation rates (Fig. S2c) and low-level PV coincide to some extent, which is consistent with diabatic PV production.

The upper-level PV anomalies and the WCB outflow masks are illustrated in Fig. S2g-i. At 18 UTC on 4 January (Fig. S2g), i.e., after the cyclone has strongly intensified, WCB trajectories arrive in the upper troposphere, spread out, and fill the entire amplifying upper-level ridge. The majority of the WCB outflow is formed by anticyclonically curved trajectories (see Sect. 2.2.2 for details concerning the mask calculation for the different branches). Only a small region in the southwest corresponds to the outflow of the cyclonic WCB branch. In the center of the WCB outflow mask, northeast of the cyclone center, a moderate negative PV anomaly has developed with values around -1.5 pvu. The ULPVA (median of the PV anomaly between 200–375 hPa within the WCB outflow mask, see Sect. 2.2.3), in the outflow of the anticyclonic branch equals -0.5 pvu, while it is strongly positive (3.4 pvu) in the small outflow region of the cyclonic WCB branch, which coincides with the upper-level trough. Twelve hours later (Fig. S2h), due to the northward progression of the ridge and the intensified WCB outflow, the negative PV anomaly has intensified in terms of its area and amplitude. A large part of the upper-level ridge is characterized by an upper-level PV anomaly with values below -2.5 pvu, which aligns almost exactly with the outflow region of the anticyclonic WCB branch (ULPVA$= -2.1$ pvu). Similar to the previous time instance, the WCB outflow west of the cyclone center is formed mainly by the cyclonic branch and is associated with a positive ULPVA of 1.7 pvu. Weak or even positive ULPVA at relatively low latitudes are linked to the equatorward reduction of the climatological PV at upper levels and are consistent with Madonna et al. (2014). A day later, at 06 UTC on 6 January (Fig. S2i), most of the WCB outflow mask is located in the upper-level ridge that developed downstream of the cyclone and is mainly formed by the anticyclonic WCB branch. Inside the outflow mask of the anticyclonic branch, the ULPVA equals -2.2 pvu, while the minimum of the entire PV anomaly has values below -2.5 pvu. Similar to the previous time step, in the westernmost part of the WCB outflow below the upper-level trough, no or only a weak negative PV anomaly is discernible. This part of the WCB outflow is largely formed by the cyclonic

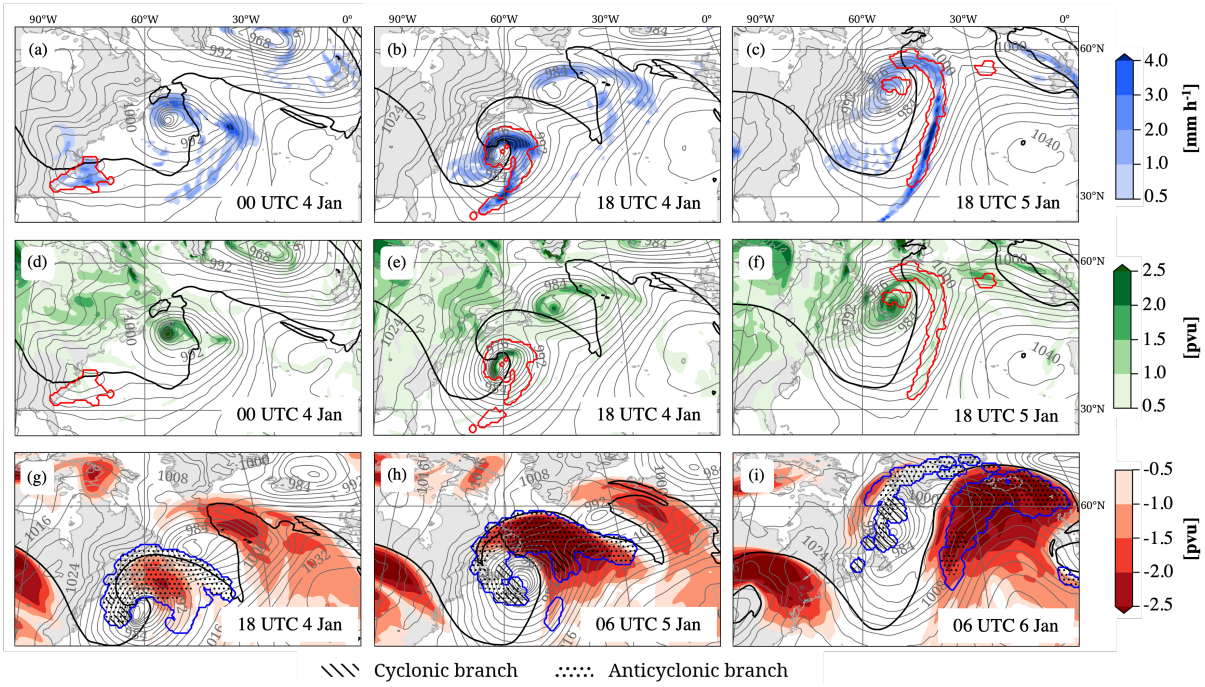

Figure S2. WCB-related impacts of Case 1 in terms of (a-c) precipitation rate (mm h^{-1}, blue shading), (d-f) low-level PV (pvu, green shading), and (g-i) upper-level PV (pvu, red shading) as well as the location of the WCB ascent and outflow masks (red and blue contours, respectively), SLP (grey contours every 4 hPa) and 2-pvu contour on 320 K (pvu, black line). The hatching in the WCB outflow mask indicates the outflow of the cyclonic (dashed) and anticyclonic (dotted) WCB branches (see text for details). All fields are shown at the times indicated in the lower right of the panels. Note that times differ when showing the WCB ascent (a-f) and WCB outflow (g-i).

WCB branch with a ULPVA of 0.6 pvu in its outflow region. To conclude, we found that both the characteristics and impacts associated with the investigated WCB co-evolve during the cyclone life cycle.

S1.3 Evolution of WCB metrics

We now quantify the characteristics and impacts of the WCB according to Sect. 2.2.3 and investigate their temporal evolution along the entire cyclone life cycle. Figure S3a shows the central pressure and deepening rate of the cyclone, which was first detected at 09 UTC on 3 January 1989. After an initial weak intensification, the deepening rate reaches about 3.4 Bergeron in the 24-h window around 05 UTC on 4 January, consistent with Neiman and Shapiro (1993). The cyclone reaches its minimum SLP of 942 hPa at 01 UTC on 5 January and gradually weakens over the following five days (partially shown). The WCB associated with this very intense cyclone also evolved with time. As already indicated in Fig. S1, the intensity of the WCB varied with time (Fig. S3b). First, the number of trajectories in the WCB ascent mask increases for about a day before reaching a maximum of 572 trajectories at the end of the most substantial cyclone intensification period. It then gradually decreases once the cyclone has reached its minimum pressure. The intensity of the WCB outflow evolves similarly but is delayed by about 12 h and shows a second local maximum during cyclone decay. At 18 UTC on 5 January, a maximum of 804 trajectories define the WCB outflow mask. In terms of ascent rate, the largest values (136 hPa $(3\,h)^{-1}$) occur at the time of maximum intensity of the WCB ascent (Fig. S3c). The ascent rates were distinctively lower (< 52 hPa $(3\,h)^{-1}$) at the early stages of the WCB evolution. As previously seen in Fig. S1a, the WCB first ascends without a distinct ascent curvature, but with time, the share of anticyclonically ascending trajectories increases until it reaches 100% at 18 UTC on 6 January (Fig. S3d). The cyclonic branch, however, remains weak over the entire cyclone life cycle, and it maximizes with 10.3% about 6 h after the time of maximum

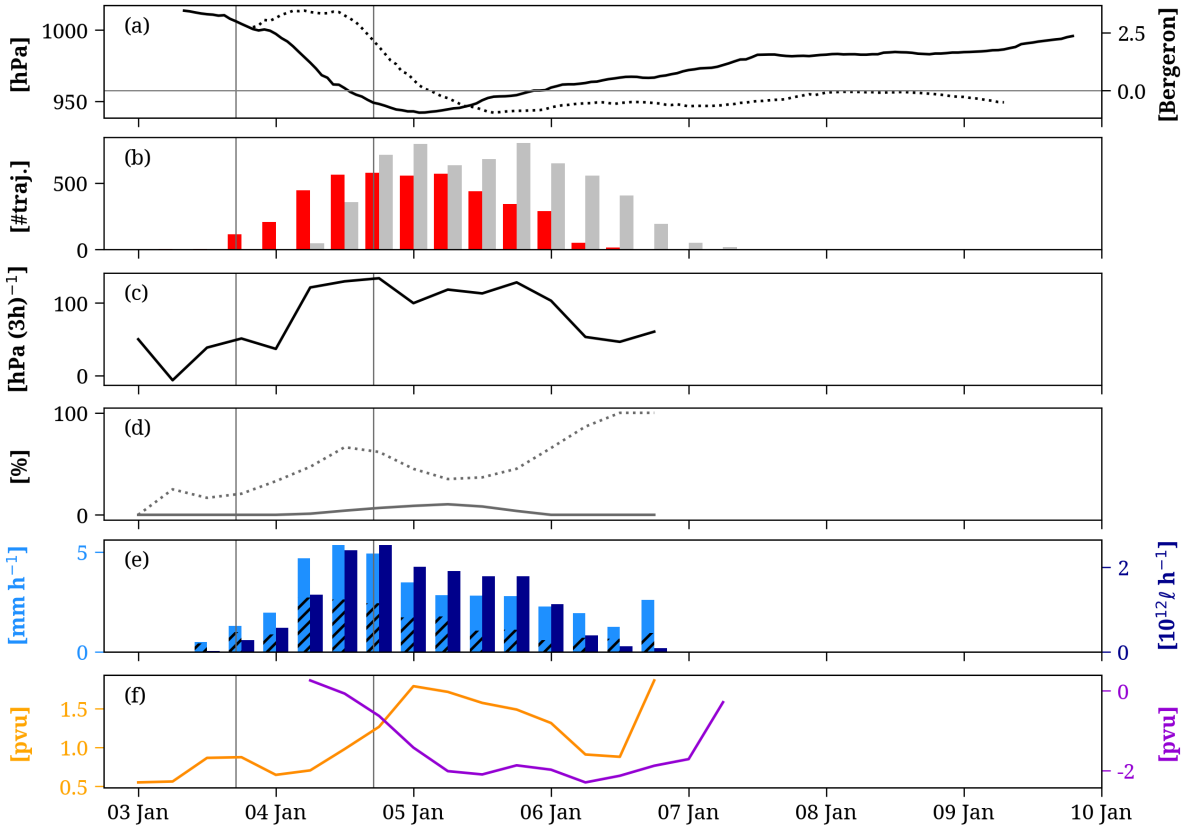

Figure S3. Temporal evolution of cyclone characteristics and WCB characteristics and impacts for Case 1: (a) the cyclone's central pressure (solid, hPa) and deepening rate in the center of 24-h window (Bergeron, dotted), (b) intensity of WCB ascent (number of trajectories, red) and outflow (number of trajectories, grey), (c) mean ascent rate (hPa (3 h)$^{-1}$), (d) percentage of cyclonically (%, solid) and anticyclonically ascending trajectories (%, dotted), (e) convective precipitation (mm h^{-1}, hatched) and PQ90 (mm h^{-1}, light blue) and PVOL (10^{12} ℓ h^{-1}, dark blue), and (f) LLPV (pvu, orange) and ULPVA (pvu, violet). Vertical lines denote the 24 h period of strongest cyclone intensification.

cyclone intensity.

The impacts of the WCB also vary with time, as shown in Fig. S3e,f. The precipitation rate, PQ90, increases rapidly during the cyclone's intensification phase and reaches a maximum of 5.3 mm h^{-1} at 12 UTC on 4 January (Fig. S3e, light blue). This peak value occurs along the bent-back front 6 h before the field shown in Fig. S2b. Afterward, the precipitation intensity slowly weakens (see also Fig. S2c). The relative share of convective precipitation decreases steadily with time along the cyclone life cycle, indicating that embedded convection is most prominent in the early phase of the cyclone when it is located at low latitudes. The precipitation volume, PVOL, reaches a maximum value of $2.5 \cdot 10^{12}$ ℓ h^{-1} towards the end of the main cyclone intensification phase at 18 UTC on 4 January (Fig. S3e, dark blue). Considering PV, during the cyclone's intensification phase, LLPV increases to maximum values above 1.5 pvu (Fig. S3f, orange line). This PV is diabatically produced and related to the strong precipitation formation near the cyclone center within the WCB ascent mask (Fig. S2e). LLPV values decrease once the cyclone reaches its minimum pressure. The brief increase in LLPV at 18 UTC on 6 January is not robust, as only a few WCB trajectories ascend at this time. At upper levels, the ULPVA intensifies rapidly in the 24 h after 06 UTC on 4 January, simultaneously with the intensity of the WCB outflow. This intensification of ULPVA was also apparent in Fig. S2g,h. The most intense ULPVA (−2.3 pvu) occurs at 06 UTC on 6 January, 36 h after the time of maximum cyclone intensity (Fig. S2i).

Thereafter, the ULPVA weakens.
As will become clearer when discussing the climatological results in Sect. 4, the WCB of the IOP4 cyclone was very intense in terms of the number of WCB trajectories, the ascent rate, precipitation rate, and volume, as well as LLPV before the cyclone reached its deepest SLP. At upper levels, the WCB outflow intensity increased simultaneously with the intensity of the ULPVA, both peaking 24–36 h after the cyclone reached its minimum SLP.

S2 Case 3: November 1992, North Atlantic

The application of the Lagrangian perspective to define and investigate WCBs from analysis data was first introduced by Wernli and Davies (1997), who applied Lagrangian selection criteria to a large set of trajectories and thereby identified WCBs as coherent bundles of trajectories in cyclones. Selecting trajectories that either experienced a strong pressure decrease, strong moisture decrease, or a strong increase in potential temperature resulted in very similar WCBs. In Wernli (1997), the authors investigated in detail a cyclone that formed in the North Atlantic in November 1992, which was associated with two WCBs, one ascending in the vicinity of the cyclone center and the other one along the trailing cold front. At upper levels, both airstreams split into anticyclonic and cyclonic branches, with the share of cyclonically ascending trajectories increasing with time. The number of trajectories that fulfilled the ascent criterion varied with time, with the largest number of WCB trajectories identified between 12 UTC on 22 November and 12 UTC on 24 November, i.e., during the main period of cyclone deepening. The same cyclone was investigated by Rossa et al. (2000), who focused on the formation of a prominent PV-tower associated with this cyclone. They showed that latent heating in ascending trajectories and associated diabatic PV production was mainly responsible for the middle and lower parts of the PV-tower. The ascending trajectories associated with the PV-tower's middle part resembled one of the WCBs identified by Wernli (1997). In the following, we will revisit this cyclone and apply our methods to quantify the characteristics and impacts of this well-studied WCB and investigate how they evolved along the cyclone life cycle.

S2.1 WCB characteristics

The cyclone formed in a complex synoptic situation, which complicates the association of WCB trajectories to the cyclone in the early phase of its life cycle. As described by Wernli (1997) and illustrated in Fig. S4a, the cyclone develops between 00 and 06 UTC on 22 November 1992 from a frontal wave that is located at 25°W 45°N and south of the mature cyclone at 30°W and 60°N. At upper levels, an elongated high-PV trough extends from about 25°N to 60°N. WCB trajectories ascend between 20°N to 50°N and ahead of almost the entire length of the PV streamer, in agreement with Wernli (1997). All of these trajectories are combined into one WCB, which ascends at this moment without a distinct curvature. At upper levels, the WCB trajectories flow into the ridge that develops downstream of the cyclone. In the following 1.5 days, the cyclone intensifies rapidly and moves poleward while the ridge downstream of the cyclone intensifies (Fig. S4b). The WCB trajectories start at low latitudes but mainly ascend further northward and east of the cyclone in a T-shaped region, consistent with the cyclone's intense bent-back front (Rossa et al., 2000). WCB trajectories ascending at latitudes south of 60°N ascend mainly without a distinct curvature, while trajectories ascending at higher latitudes first ascend cyclonically but then turn anticyclonically at higher altitudes. A small fraction of the WCB ascends strictly cyclonically toward the cyclone center. Figure S4b also shows impressively the large area extending from Greenland to eastern Europe covered by the WCB outflow.

S2.2 WCB impacts

Figure S5 shows the WCB-related impacts in the region of WCB ascent (Fig. S5a-f) and WCB outflow (Fig. S5g-i). At 00 UTC on 22 November (Fig. S5a), the elongated PV trough southwest of the mature cyclone leads to the formation of an elongated band of precipitation along its eastern flank. The precipitation formation coincides almost entirely with the WCB ascent mask. Precipitation rates are especially intense at low latitudes ($> 4\,\mathrm{mm\,h^{-1}}$). 18 h later (Fig. S5b), the WCB ascends not only along the cold front but also near the center of the emerging cyclone located at 20°W and 55°N. Similar to the previous time step, the majority of the cyclone's precipitation coincides with the WCB ascent mask, and the most intense precipitation rates occur

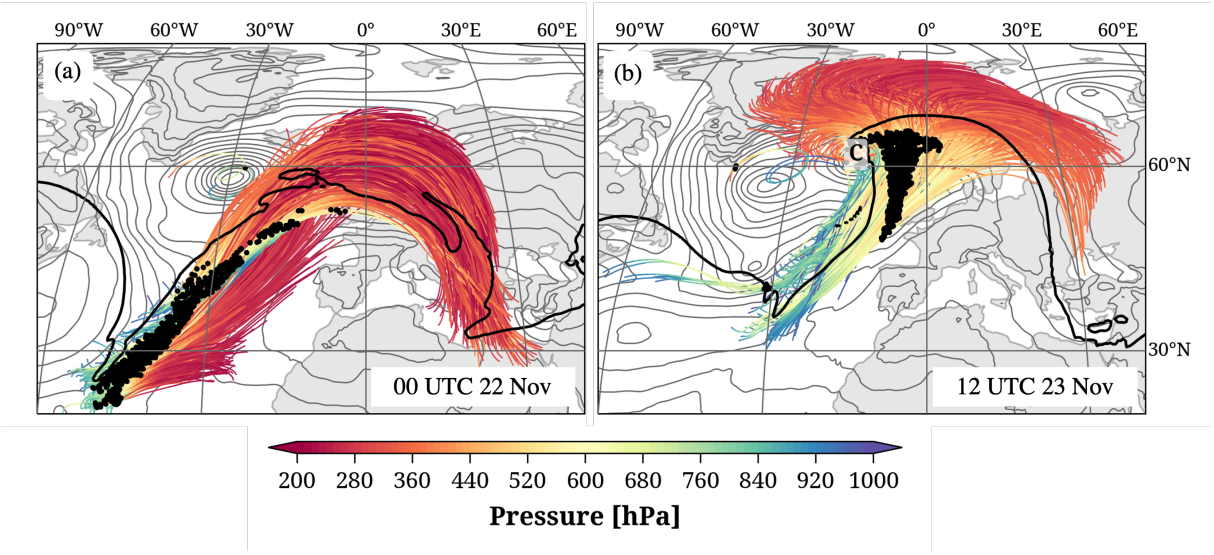

Figure S4. As Fig. S1 but for Case 3 trajectories that are located in the WCB ascent pressure range at (a) 00 UTC on 22 November and (b) 12 UTC on 23 November 1992.

along the cold front, consistent with Wernli (1997). Weak precipitation along the cyclone's warm front is not related to the WCB ascent. Another 18 h later (Fig. S5c), the cyclone has noticeably intensified, and the WCB ascent mask, defined by the trajectories shown in Fig. S4b, coincides with weak precipitation rates along the weakening cold front and with more intense precipitation rates along the warm and bent-back fronts.

The cyclone forms at 00 UTC on 22 November in proximity to a small region of enhanced low-level PV (1.5–2 pvu, Fig. S5d), located at 20°W and 47°N. The region of WCB ascent, mainly located southwest of the local PV maximum, aligns with a band of mildly enhanced low-level PV. In contrast, 18 h later (Fig. S5e), the region of intense precipitation along the cyclone's cold front is also associated with a band of distinctively enhanced low-level PV (1.5–2 pvu). The diabatically produced PV linked to the precipitation formation along the ascending WCB is consistent with findings by Rossa et al. (2000). In addition, low-level PV is also enhanced near the cyclone center, coinciding with intense precipitation rates. After the strong cyclone intensification (Fig. S5f), low-level PV is mainly enhanced along the warm front and near the cyclone center but less intense along the cold front. The strongly enhanced PV values in the cyclone center formed the lower part of the PV-tower described by Rossa et al. (2000). The WCB ascent mask coincides with the described regions of enhanced PV inside the cyclone. At this moment, precipitation rates and low-level PV values correlate less than at the previous time step. As we only take PV values between 750–950 hPa into account, enhanced PV values above this pressure range will not be detected.

The WCB arrives at upper levels first at 18 UTC on 22 November (Fig. S5g) in an elongated band that extends from the southern end of the PV trough to the northern end of the ridge that develops downstream of the cyclone. The intense negative PV anomaly (< -2.5 pvu) associated with the ridge coincides with the WCB outflow of the anticyclonic branch, which is characterized by a ULPVA of -2.3 pvu. In the following 1.5 days (Fig. S5h), the negative PV anomaly intensifies while the ridge moves poleward and eastward. Similar to the previous time instance, the PV anomaly coincides strongly with the outflow of the anticyclonic branch (ULPVA$= -2.1$ pvu). The outflow of the cyclonic branch extends to a region of weak/no upper-level PV anomalies in the west of the ridge and towards the cyclone center. As a result, the ULPVA inside the outflow mask of the cyclonic branch equals 0.4 pvu. The interpretation of the slightly positive value is that here the WCB outflow is at a lower altitude compared to the anticyclonic branch, and therefore the tropopause is close to its climatological position (leading to a weak anomaly in the layer considered for the calculation of ULPVA). At 00 UTC on 24 November (Fig. S5i), the ridge extends towards the west due to the cyclonic WCB branch that advects anomalously low-PV air from the ridge towards the west. Thus, the ULPVA inside the outflow of the cyclonic branch becomes slightly negative (-0.4 pvu). In contrast, the outflow of the

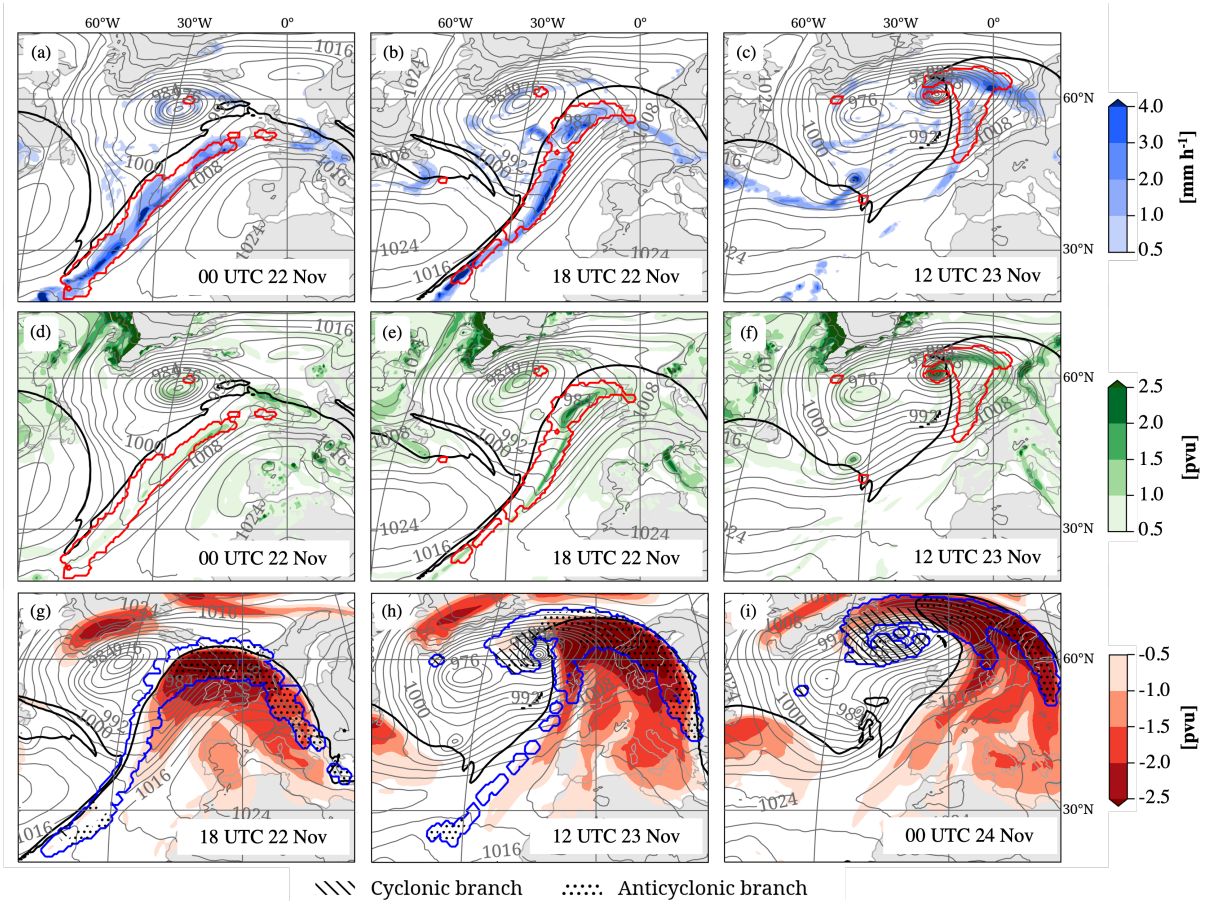

Figure S5. As Fig. S2 but for Case 3 (19–25 November 1992) at the times indicated in the lower right of each panel. Note that times differ when showing the WCB ascent (a-f) and WCB outflow (g-i).

anticyclonic branch is still associated with a strongly negative ULPVA of -2.7 pvu.

S2.3 Evolution of WCB metrics

The temporal evolution of the cyclone, as well as the characteristic and impact metrics that describe the WCB, are shown in Fig. S6. The cyclone is first discernible at 03 UTC on 22 November 1992 with a central pressure of 995.4 hPa (Fig. S6a). After an initial weak intensification phase of about a day, the central pressure decreases rapidly at 00 UTC on 23 November. The cyclone reaches its minimum pressure (938.3 hPa) at 17 UTC on 23 November and afterward weakens slowly. The rapid decrease in pressure results in a maximum deepening rate of 1.9 Bergeron at 19 UTC on 22 November. As previously described, the ascent of the WCB is first mainly driven by upper-level forcing and later influenced by the cyclone. The WCB ascent mask is first identified at 12 UTC on 19 November (red bars, Fig. S6b), 2.5 days before the genesis of the cyclone. The temporal delay is linked to the manual attribution of the trajectories to the later emerging cyclone. In the initial phase of the WCB evolution, only a small number of trajectories ascend at low latitudes south of the developing PV trough (not shown). Only when the WCB starts to ascend ahead of the PV trough at around 00 UTC on 21 November the WCB intensity increases distinctively. The WCB reaches its maximum intensity at 06 UTC on 22 November with 1136 trajectories and remains very intense for the

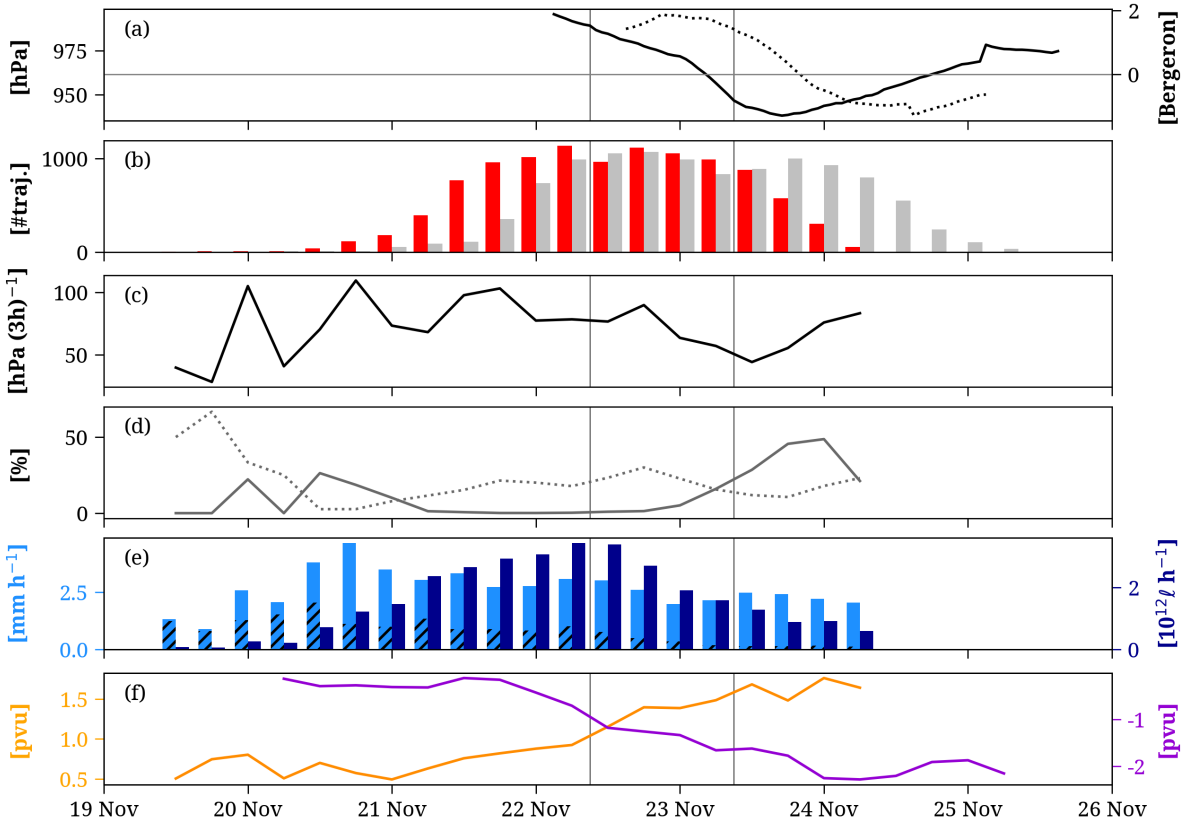

Figure S6. As Fig. S3 but for the cyclone and WCB in Case 3 (19–25 November 1992). Please note the change of scales.

following day, coinciding with the cyclone's main intensification period. After the cyclone's most rapid intensification period, the WCB weakens and vanishes after about a day. A small number of WCB trajectories arrive in the WCB outflow region at 06 UTC on 20 November (grey bars, Fig. S6b). With a delay of approx. one day relative to the WCB ascent, also the WCB outflow intensity increases. About 1000 trajectories remain in the WCB outflow region until 00 UTC on 24 November, when the number of trajectories decreases gradually.

While the incipient WCB ascends at low latitudes with more than $100\,\mathrm{hPa\,(3\,h)^{-1}}$, the ascent rate decreases to $44\,\mathrm{hPa\,(3\,h)^{-1}}$ after the cyclone's main intensification period when the WCB ascent mask is located at higher latitudes. The decline in the ascent rate of the WCB could potentially be attributed to the generally greater probability of convective and rapid ascent occurring at lower latitudes. However, we did not explore this hypothesis further. The curvature of the WCB also evolves with time, as qualitatively described above. The WCB starts as a mainly straight flow; large variations at early stages are caused by a small number of trajectories and are thus statistically less robust (Fig. S6d). While the number of trajectories increases drastically, the relative intensity of the W1 and W2 branches remains relatively constant. Towards the end of the cyclone's intensification period, the share of W2 starts to increase, while W1 remains at a relatively constant percentage. This finding is consistent with Wernli (1997), who already described the split of the WCB and an increase in the intensity of the cyclonic branch with time. The decreased intensity of the W2 branch at 06 UTC on 24 November is linked to the relatively small total number of trajectories and, thus, less robust statistics.

Figure S5 already showed that the WCB ascent mask coincides well with the cyclone-related precipitation. PQ90 is most intense ($4.6\,\mathrm{mm\,h^{-1}}$, light blue bars in Fig. S6e) at 18 UTC on 20 November, in the early stages of the WCB's evolution, when

it ascended mainly at low latitudes. The northward movement is associated with a decrease in PQ90 and a decline in the share of convectively formed precipitation. However, PVOL (dark blue bars in Fig. S6e) peaks later at the beginning of the cyclone's intensification period. This delay is due to the increased WCB ascent mask area with WCB intensity. Before the WCB intensity increases distinctively, LLPV remains between 0.5–1 pvu for the first 1.5 days (orange line, Fig. S6f). Once the WCB starts to intensify noticeably, LLPV increases until it reaches 1.7 pvu briefly after the main cyclone intensification period. The diabatic PV production and the increase of the Coriolis parameter towards the north both contribute to the increase in LLPV. At upper levels, ULPVA (purple line, Fig. S6f) remains weak until 12 UTC on 21 November, when the first significant amount of air transported by the WCB reaches higher altitudes. The ULPVA then intensifies to about -2.3 pvu at 00 UTC on 24 November and persists until the WCB outflow mask disappears.

In summary, the importance of the WCB in this case study for the precipitation formation and diabatic PV formation, as described by Wernli (1997) and Rossa et al. (2000), were also captured by our method, as well as the increase in the intensity of the cyclonic branch as qualitatively described by Wernli (1997). Furthermore, the WCB outflow was found to align with a ULPVA that intensified significantly along the cyclone life cycle.

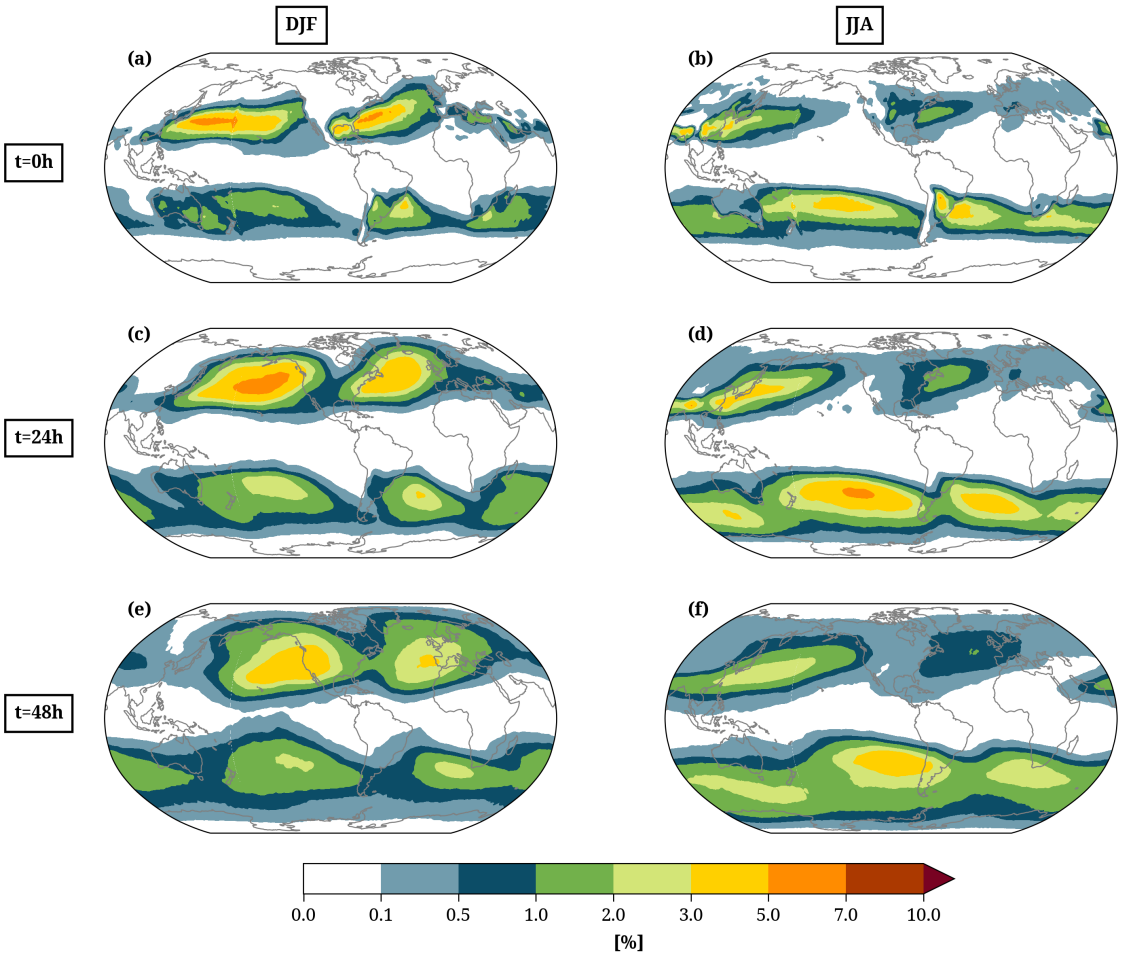

Figure S7. 42-year (1980–2022) climatology of the frequency (%) of WCB trajectories in (left column) DJF and (right column) JJA, at (a, b) $t = 1$ h, (c, d) $t = 24$ h and (e, f) $t = 48$ h.

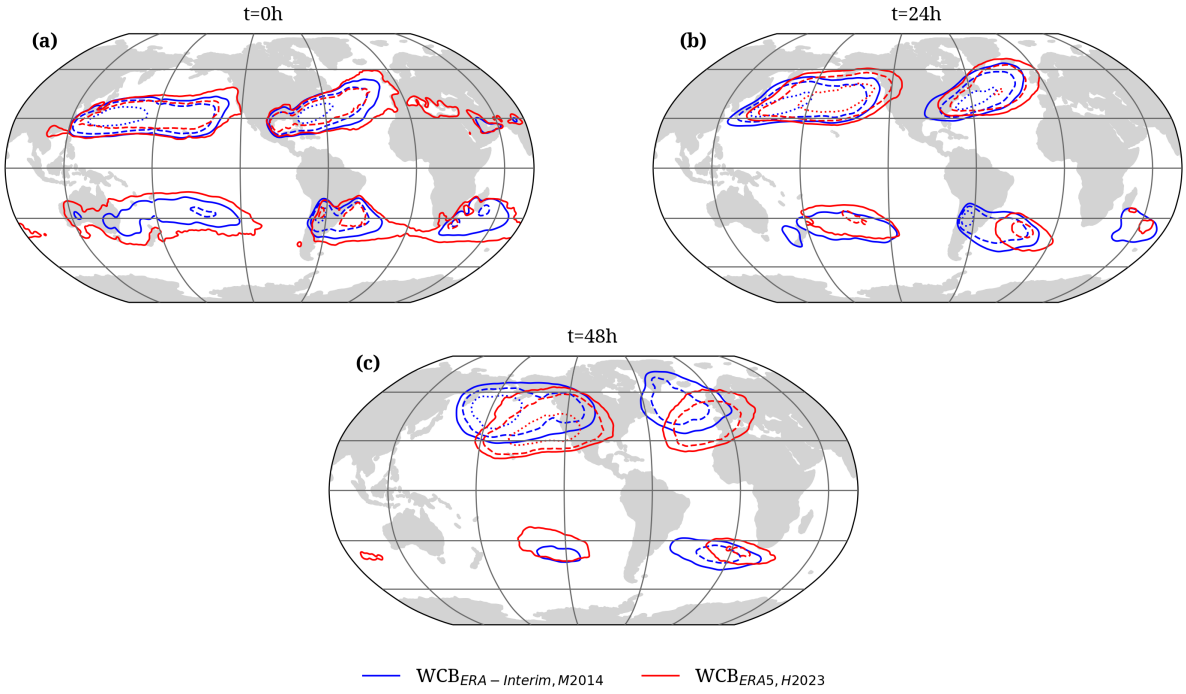

Figure S8. Regions of frequent WCB at (a) $t = 0$ h, (b) $t = 24$ h and (c) $t = 48$ h in winter (December–February). The blue contours correspond to WCB trajectories calculated in ERA-Interim and the WCB definition used by Madonna et al. (2014) for the time period 1980–2015, while the red contours correspond to WCB trajectories calculated in ERA5 and the adapted WCB definition described by Heitmann et al. (2023) for the time period 1980–2022. Due to the different numbers of trajectories and different absolute frequency values, the contours denote the 90^{th} (solid), 95^{th} (dashed) and 99^{th} (dotted) percentile of the ERA-Interim and ERA5 field.

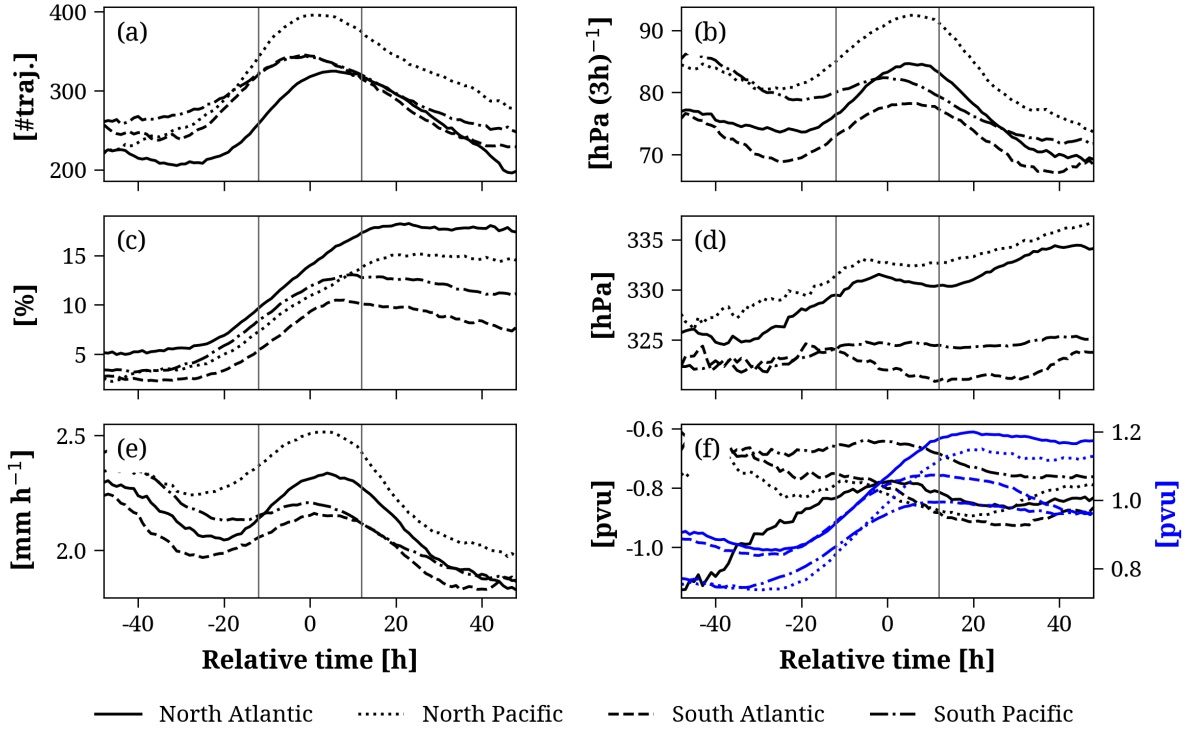

Figure S9. Mean (solid and dotted line) and 50% confidence interval (shading) of the cyclone and WCB metrics centered around the time of maximum cyclone intensification ($t_{rel} = 0$ h). The solid and dashed lines correspond to the mean value of WCB associated with cyclones with a maximum $\Delta\text{SLP}_B > 0$ and $\Delta\text{SLP}_B > 1$, respectively. (a) Cyclone's central pressure (hPa), (b) WCB intensity of the ascent (black) and outflow mask (number of trajectories, grey), (c) WCB ascent rate (hPa (3 h)$^{-1}$), (d) percentage of cyclonic (black) and anticyclonically ascending trajectories (%, grey), (e) total precipitation rate (mm h^{-1}, light-blue) and total precipitation volume ($10^{12}\ell$ h^{-1}, dark-blue), and (f) low-level PV (pvu, orange) and upper-level PV anomaly (pvu, violet) for all WCBs ascending in the NA in DJF between 1980–2022. Vertical lines denote the 24-hour period of strongest cyclone intensification.

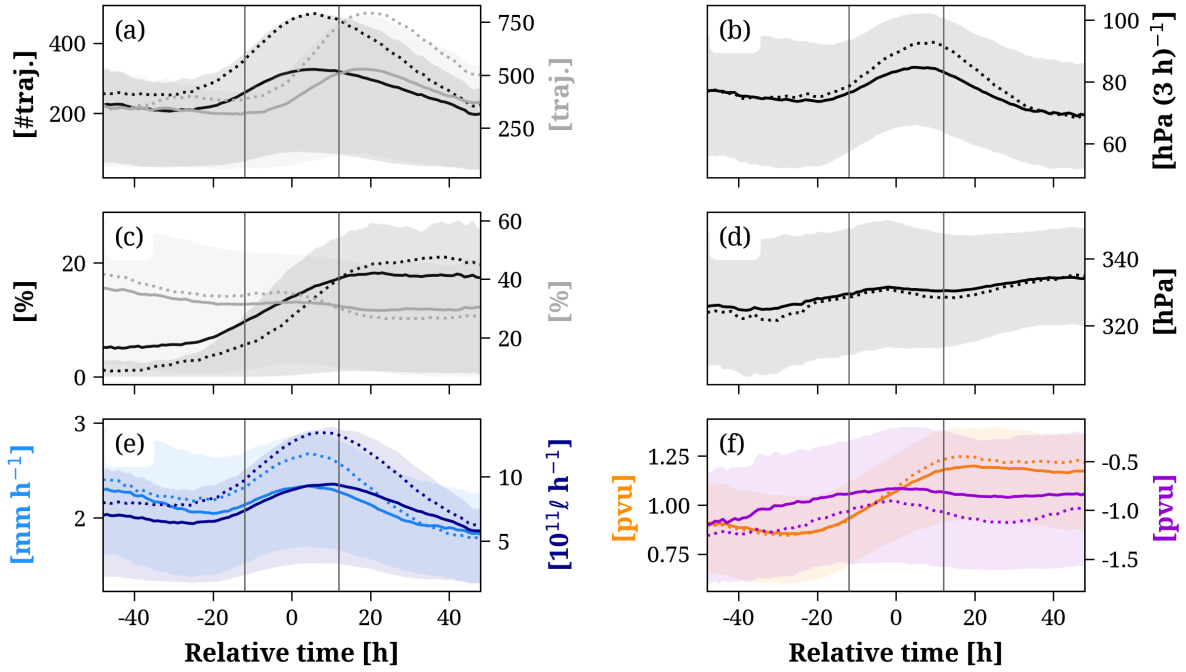

Figure S10. Similar to Fig. 10 and Fig. S10 but for the mean evolution of WCBs ascending in the North Atlantic (solid), North Pacific (dotted), South Atlantic (dashed) and South Pacific (dash-dotted) in the respective winter season of (a) cyclone's central pressure (hPa), (b) WCB intensity of the ascent (number of trajectories), (c) WCB ascent rate (hPa (3 h)$^{-1}$), (d) percentage of cyclonically ascending trajectories (%), (e) total precipitation rate (mm h^{-1}) and (f) low-level PV (pvu) and upper-level PV anomaly (pvu, blue). All WCBs associated with cyclones with a maximum $\Delta\mathrm{SLP}_B > 0$ were taken into account.

The climatological evolution of the characteristics and impacts of WCBs ascending in the respective winter season in the North Pacific (105°E–110°W, 20°N–80°N), South Atlantic (65°W–10°E, 15°S–60°S) and South Pacific (150°E–70°W, 15°S–60°S) is shown in Fig. S10. North Pacific WCBs show higher values of WCB intensity, ascent rate, and PQ90 compared to WCBs ascending in other regions (Fig. S10a,b,e). The outflow of WCBs ascending in the Southern Hemisphere reaches higher altitudes than in the Northern Hemisphere (Fig. S10d). The increase in the share of cyclonically ascending trajectories (Fig. S10c) is similar in all regions but reaches the largest values in the North Atlantic. While the LLPV increases most strongly in the North Pacific (Fig. S10e), the ULPVA becomes most intense in the South Atlantic (Fig. S10f).

References

Madonna, E., Wernli, H., Joos, H., and Martius, O.: Warm conveyor belts in the ERA-Interim dataset (1979–2010). Part I: Climatology and potential vorticity evolution, J. Clim., 27, 3–26, https://doi.org/10.1175/JCLI-D-12-00720.1, 2014.

Neiman, P. J. and Shapiro, M.: The life cycle of an extratropical marine cyclone. Part I: Frontal-cyclone evolution and thermodynamic air-sea interaction, Mon. Weather Rev., 121, 2153–2176, https://doi.org/10.1175/1520-0493(1993)121<2153:TLCOAE>2.0.CO;2, 1993.

Neiman, P. J., Shapiro, M., and Fedor, L.: The life cycle of an extratropical marine cyclone. Part II: Mesoscale structure and diagnostics, Mon. Weather Rev., 121, 2177–2199, https://doi.org/10.1175/1520-0493(1993)121<2177:TLCOAE>2.0.CO;2, 1993.

Rossa, A. M., Wernli, H., and Davies, H. C.: Growth and Decay of an Extra-Tropical Cyclone's PV-Tower, Meteorology and Atmospheric Physics, 73, 139–156, https://doi.org/10.1007/s007030050070, 2000.

Thorncroft, C., Hoskins, B., and McIntyre, M.: Two paradigms of baroclinic-wave life-cycle behaviour, Q. J. Roy. Meteor. Soc., 119, 17–55, https://doi.org/10.1002/qj.49711950903, 1993.

Wernli, H.: A Lagrangian-based analysis of extratropical cyclones. II: A detailed case-study, Q. J. Roy. Meteor. Soc., 123, 1677–1706, https://doi.org/10.1002/qj.49712354211, 1997.

Wernli, H. and Davies, H. C.: A Lagrangian-based analysis of extratropical cyclones. I: The method and some applications, Q. J. Roy. Meteor. Soc., 123, 467–489, https://doi.org/10.1002/qj.49712353811, 1997.